Article

Direct and stable hydrogenation of CO$_2$ to aromatics over a tandem catalyst Zn$_{0.1}$Ti$_{0.9}$O$_x$/HZSM-5

Zn$_{0.1}$Ti$_{0.9}$O$_x$/ZSM-5
3 MPa 320 °C

Aromatics ~67%
100 h stability

Junfu Zhou, Yuting
Miao, Hongxin
Ding, Yuanhang
Ren, Lin Ye, Bin
Yue, Heyong He

yelin@fudan.edu.cn (L.Y.)
yuebin@fudan.edu.cn (B.Y.)
heyonghe@fudan.edu.cn (H.H.)

Highlights
Direct conversion of CO$_2$ to
aromatics over the tandem
Zn$_{0.1}$Ti$_{0.9}$O$_x$/HZSM-5-(100)
catalyst

Appropriate density and
strength of acid sites
induce a high aromatics
selectivity

The formate route
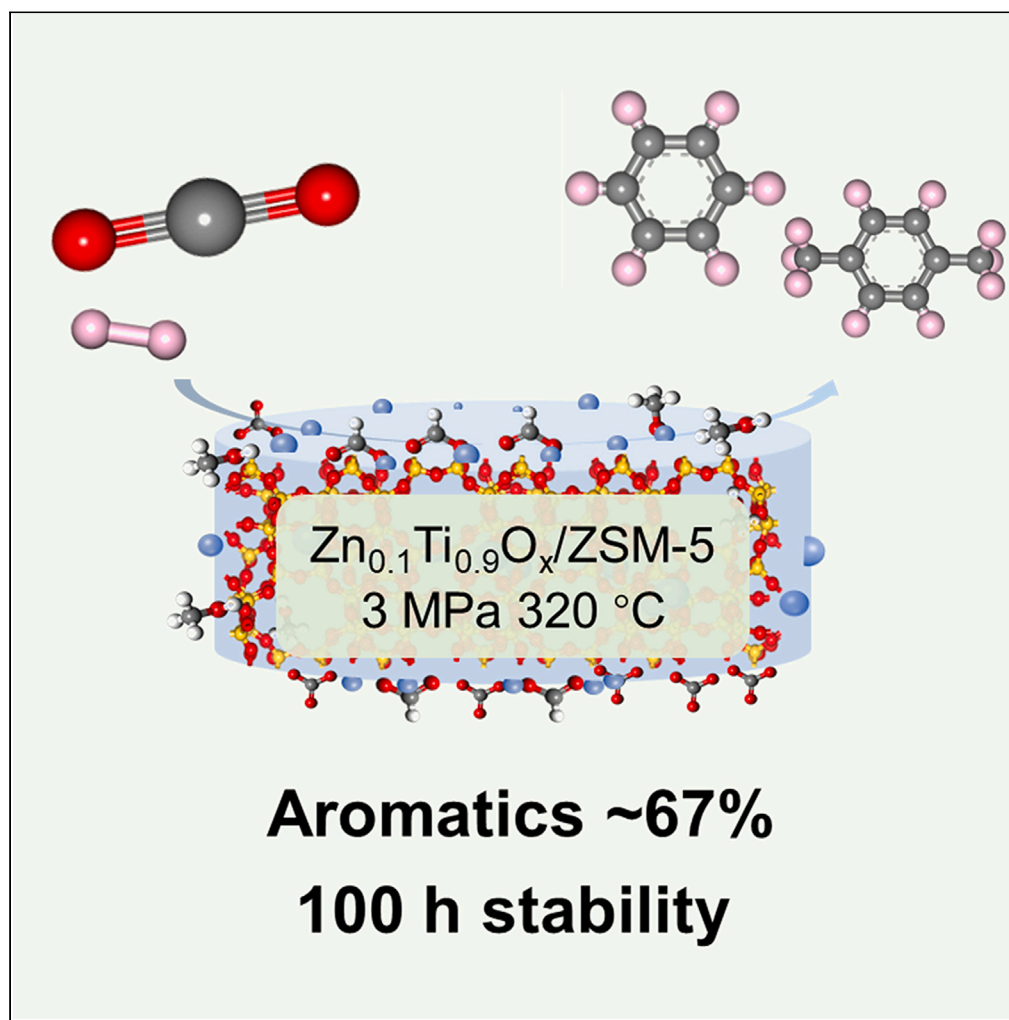dominates the direct CO$_2$
to aromatics process

Article

Direct and stable hydrogenation of CO_2 to aromatics over a tandem catalyst $Zn_{0.1}Ti_{0.9}O_x$/HZSM-5

Junfu Zhou,[1,2] Yuting Miao,[1,2] Hongxin Ding,[1] Yuanhang Ren,[1] Lin Ye,[1,3,*] Bin Yue,[1,*] and Heyong He[1,*]

SUMMARY

Direct and stable conversion of CO_2 to aromatics (CTA) is an attractive route for reducing CO_2 emissions. However, due to the chemical inertness of CO_2, direct CTA reaction with high aromatics selectivity is still challenging. In this work, a tandem catalyst $Zn_{0.1}Ti_{0.9}O_x$/HZSM-5 with appropriate density and strength of acid sites exhibits a high aromatics selectivity of 67.2% and long-term stability over 100 h. Furthermore, the total selectivity of benzene, toluene, and xylene achieves 24.1% over $Zn_{0.1}Ti_{0.9}O_x$/HZSM-5 with a modified hydrophilic surface. In addition, the CTA via the formate route has been determined in this reaction system.

INTRODUCTION

The CO_2 emission associated with global warming and extreme climate has attracted international concern.[1,2] CO_2 can be considered as an abundant carbon feedstock instead of waste from the view of carbon capture and utilization (CCU) technologies. In principle, CO_2 can be transformed into various value-added chemicals,[3] such as aromatics, a vital building block in the chemical industry.

Generally, aromatics refer to hydrocarbons containing a benzene ring in the structure. They are essential raw materials for the polymer synthesis industry, which can produce synthetic rubber, plastics and fibers.[4] Benzene, toluene and xylene (known as BTX) are more valuable in the family of aromatics, of which p-xylene (PX) is the primary raw material of polyethylene terephthalate (PET). Usually, aromatics are produced from steam reforming of naphtha and catalytic petroleum cracking. Alternative production routes for aromatics via non-oil-based processes are urgently needed to slow the rapid depletion of the limited petroleum resources.[5,6] In recent decades, there have been two main syngas routes for aromatics production. One is the syngas indirect route, which is a mature industrial process. First, methanol is synthesized through the Fischer–Tropsch process. Then, methanol converts to aromatics over zeolites through the methanol-to-aromatics (MTA) process. However, the MTA process suffers from rapid deactivation of the catalysts due to coke deposition.[7–9] The other is the syngas direct route (syngas to aromatics, STA)[10] The strategy of metal oxides coupled with zeolite (OX-ZEO) has broken the restriction of Anderson-Schulz-Flory distribution and obtained high aromatics selectivity.[5,6,11,12] Based on the OX-ZEO system successfully employed in syngas conversion, the tandem system has also been applied to the CTA process.[8,13,14] Li et al. achieved the highest aromatics selectivity up to 73% at CO_2 single-pass conversion of 14%, and the BTX selectivity is around 10% over a ZnZrO/ZSM-5 catalyst.[9] Liu et al. utilized the $ZnAlO_x$ and ZSM-5 catalysts, yielding a high aromatics selectivity of 73.9% and a BTX selectivity of about 20%.[14] According to the overreaction of formed BTX on the external surface of zeolites, the heavy aromatics that contain at least 9 carbon atoms (named C_{9+}) are easily created, which decreases the proportion of BTX in aromatics. As a result, the BTX selectivity in the overall CO_2 hydrogenation reaction is difficult to exceed 20%.[8] Tsubaki et al. found that the proper density and strength of the acid sites in zeolite could dramatically improve the aromatics distribution and prolong catalyst stability.[8,14–16] Also, methanol is considered to be one of the critical intermediates for the CTA reaction. Thus, combining the OX with high methanol productivity and the ZEO with precisely modified acidity is essential for the high selectivity of aromatics (BTX) and long-term stability of the catalysts.

In our previous work, a robust binary metal oxide $Zn_{0.1}Ti_{0.9}O_x$ was developed as a CO_2 to methanol catalyst. It exhibited up to 85.6% methanol selectivity and comparable space-time yield ($0.424\ g_{MeOH}\ g_{cat.}^{-1}\ h^{-1}$) to the benchmark Cu-ZnO-Al_2O_3 ($0.575\ g_{MeOH}\ g_{cat.}^{-1}\ h^{-1}$).[17] In this work, the $Zn_{0.1}Ti_{0.9}O_x$ catalyst was further applied as the OX part of the OX-ZEO tandem catalyst coupled with a series of HZSM-5, which contains different SiO_2/Al_2O_3 ratios, for the CTA process. The factors that may affect the selectivity of aromatics, such as temperature, pressure and gas hourly space velocity (GHSV), were carefully studied. Moreover, the external acid sites of HZSM-5 were blocked by hydrophilic tetraethyl orthosilicate (TEOS) molecules to modulate the distribution of the aromatics. The stability of $Zn_{0.1}Ti_{0.9}O_x$/HZSM-5 was tested for 100 h under the best reaction condition. Also, the mechanism of CO_2 hydrogenation was investigated by in-situ DRIFTS.

RESULTS

Catalytic performance

$Zn_{0.1}Ti_{0.9}O_x$ is utilized as the metal oxide part of the tandem catalyst. $Zn_{0.1}Ti_{0.9}O_x$ shows a stable CO_2 conversion and methanol selectivity around 300°C, which matches the temperature of the MTA process.[17] Therefore, $Zn_{0.1}Ti_{0.9}O_x$ was coupled with a series of HZSM-5 as the tandem catalysts (named as $Zn_{0.1}Ti_{0.9}O_x$/HZSM-5-(x), x represents the molar ratio of SiO_2/Al_2O_3 in HZSM-5) for the direct production of aromatics via CO_2 hydrogenation.

The catalytic performances of $Zn_{0.1}Ti_{0.9}O_x$/HZSM-5-(x) for CTA reaction are shown in Figure 1 and supplemental information, Figures S1 and S2. The CO_2 conversion (blue spot) and the selectivity of CO (brown spot) decrease with the increase of the SiO_2/Al_2O_3 ratio (Figure 1A). Meanwhile, the selectivity of light alkanes drops significantly. However, the selectivity of aromatics increases first and reaches a maximum of 59% when the SiO_2/Al_2O_3 ratio is 100. With further increasing the SiO_2/Al_2O_3 ratio, the selectivity of aromatics begins to decrease. Meanwhile, the selectivity of light olefin and methanol/dimethyl ether (DME) significantly increases. Therefore, the $Zn_{0.1}Ti_{0.9}O_x$/HZSM-5-(100) with the best aromatics selectivity was further studied. The factors that affect the aromatics selectivity of $Zn_{0.1}Ti_{0.9}O_x$/HZSM-5-(100), such as the reaction temperature, pressure and GHSV were regulated. Figure 1B shows that as the reaction temperature increases, the CO_2 conversion rises linearly while the selectivity of light alkanes, C_{5+}, and methanol/DME increases. Oppositely, the selectivity of aromatics decreases with the increase in temperature. When the reaction temperature is at 320°C, the highest yield of aromatics is achieved with the single-pass conversion of CO_2 of 10.7% and the selectivity of aromatics of 67.2%. In addition, the selectivity of CO increases slightly over the $Zn_{0.1}Ti_{0.9}O_x$ catalyst with temperature increasing (Figure S3). As the previous work mentioned,[17] the CO_2 hydrogenation to methanol route is preferred and the RWGS reaction is suppressed over the $Zn_{0.1}Ti_{0.9}O_x$ catalyst. As the HZSM-5-(100) does not show activity in CO_2 hydrogenation (Figure S2). Therefore, the selectivity of CO is mainly contributed by the $Zn_{0.1}Ti_{0.9}O_x$ catalyst. Consequently, the selectivity of CO is changed slightly with temperature increasing over the $Zn_{0.1}Ti_{0.9}O_x$/HZSM-5-(100) catalyst as well. The effect of the reaction pressure was evaluated (Figure 1C). The CO_2 conversion increases as the pressure increases. However, the pressure does not affect product distribution, and the aromatics selectivity is higher than 60.0% in the testing pressure range. Considering the balance of the CO2 conversion, aromatics selectivity, and the energy input, the pressure of 3 MPa is preferred to be used as the reaction pressure. With the increase of GHSV, the CO_2 conversion decreases dramatically, along with a decrease in the selectivities of light alkanes, C_{5+} and methanol/DME (Figure 1D). The selectivity of aromatics increases with the increase of GHSV until the GHSV reaches 3000 mL $g_{cat.}^{-1}$ h^{-1}. Then, the selectivity of aromatics does not change much with a further increase in the GHSV. Here, the internal transport limitation can be negligible, as the Weisz-Prater criterion (θ_G) is 0.213 ≪ 1. GHSV is correlated with the contact time of the reactant over the catalyst. A proper GHSV means the suitable contact time of the reactant or intermediate with the catalyst will favor an increase in the selectivity of aromatics. In our studied GHSV range, the best CO_2 conversion and aromatics selectivity is achieved at a GHSV of 2250 mL $g_{cat.}^{-1}$ h^{-1}, which was comparable to the reported catalysts. (Table S1).

The long-term performance of $Zn_{0.1}Ti_{0.9}O_x$/HZSM-5-(100) was further evaluated under the optimized reaction condition (Figure 1E). The catalytic performance is stable throughout the process with the constant CO_2 conversion and aromatics selectivity. No apparent deactivation was observed after the reaction continued for 100 h, which is quite different from the quick deactivation of the MTA process.[7,8] After the long-term reaction, the used $Zn_{0.1}Ti_{0.9}O_x$/HZSM-5-(100) was further analyzed through thermal analysis and GC-MS techniques. According to the TG results (supplemental information, Figure S4A), the weight loss step appears in the range of 200–700°C, mainly attributed to the removal of deposited organic matter.[18] The weight loss of this step is about 2.0 wt %, which indicates that the carbon deposition on the $Zn_{0.1}Ti_{0.9}O_x$/HZSM-5-(100) is relatively low. The residuals on used $Zn_{0.1}Ti_{0.9}O_x$/HZSM-5-(100) were also analyzed using the GC-MS technique. (supplemental information, Figure S4B and catalyst characterization section). The results show the residuals on the external surface of the catalyst are mainly long-chain saturated alkanes and monocyclic aromatic hydrocarbons containing branched chains. The polycyclic aromatic hydrocarbons are not detected. The species on the inner surface are similar to those on the external surface. Compared to the typical MTA process, CO_2 hydrogenation takes place in a reduction atmosphere and relatively low methanol concentration, which will not favor the formation of the deactivating species such as polycyclic aromatics.[19] Therefore, the ability to suppress the formation of polycyclic aromatic hydrocarbons over $Zn_{0.1}Ti_{0.9}O_x$/HZSM-5-(100) makes its excellent long-term stability.[20–25]

The structure and acid properties of $Zn_{0.1}Ti_{0.9}O_x$/HZSM-5-(100)

The detailed structure of $Zn_{0.1}Ti_{0.9}O_x$/HZSM-5-(x) was analyzed by X-ray diffraction (XRD), field emission scanning electron microscopy (FE-SEM) and energy dispersive X-ray spectroscopic (EDS) mapping and so on. The XRD patterns show that HZSM-5-(x) samples exhibit the characteristic diffraction peaks of MFI, which means the pure phase of HZSM-5-(x) is obtained (supplemental information, Figure S5). The actual SiO_2/Al_2O_3 ratios of HZSM-5-(x) measured by X-ray fluorescence (XRF) were close to the stoichiometric values as well (supplemental information, Table S2). The HZSM-5-(x) samples show a specific surface area of around 300 m^2 g^{-1} measured by N_2 adsorption-desorption characterization. The uptake also reveals the hierarchical pore structure composed of microporous, mesopore and macropore at a low P/P_0 value (0–0.10), the type-IV hysteresis loop observed at $P/P_0 > 0.60$ and the uptake at P/P_0 value close to 1.0 in the N_2 adsorption-desorption isotherm curves, respectively (supplemental information, Figure S6).[6] The XRD pattern of $Zn_{0.1}Ti_{0.9}O_x$/HZSM-5-(100) shows both the diffraction of $Zn_{0.1}Ti_{0.9}O_x$ and HZSM-5, which indicates the $Zn_{0.1}Ti_{0.9}O_x$ and HZSM-5-(100) keep the structure of each after physical mixing process (Figure 2A). The morphology of $Zn_{0.1}Ti_{0.9}O_x$/HZSM-5-(100) was further investigated by FE-SEM (Figure 2B). The image shows that the $Zn_{0.1}Ti_{0.9}O_x$/HZSM-5-(100) contains two morphological types of samples. One is the small particle around 19 nm, and the other is the hexagonal prism around 1 μm. The EDS spectrum on the selected area illustrates the presence of Zn and Ti elements, The EDS spectrum on the
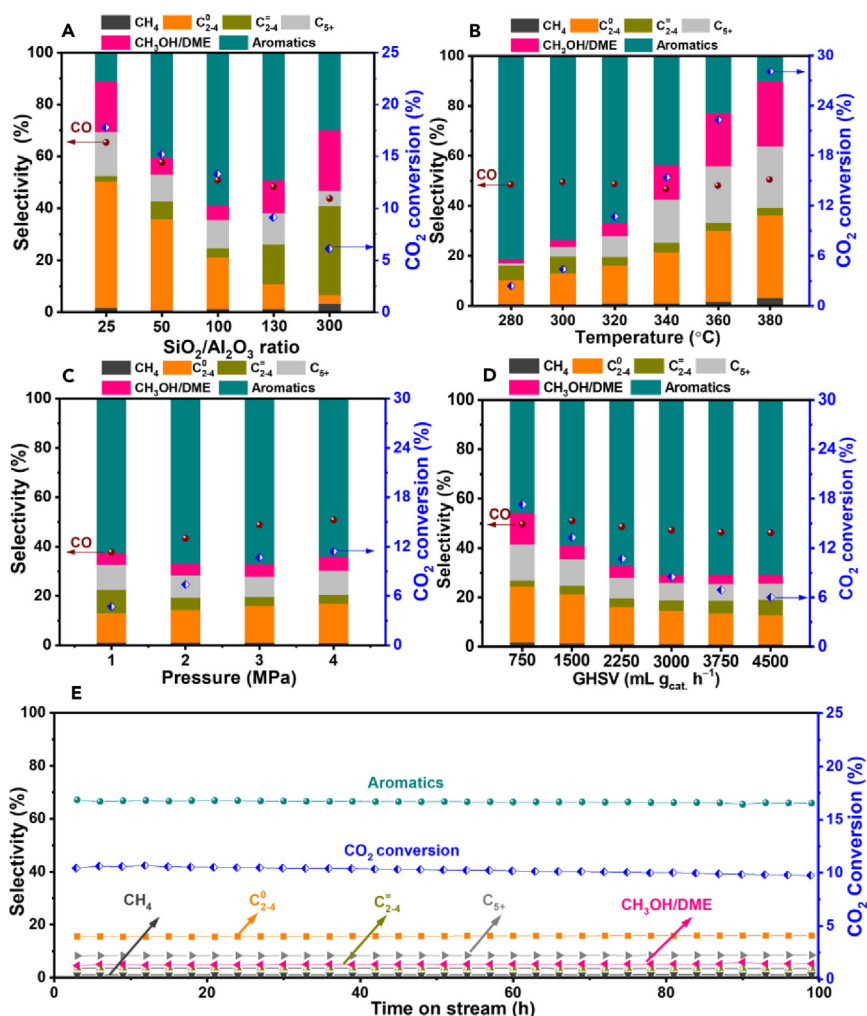
Figure 1. CO$_2$ hydrogenation over Zn$_{0.1}$Ti$_{0.9}$O$_x$/HZSM-5-(x) catalyst

(A) The catalytic performance of CO$_2$ hydrogenation to aromatics over Zn$_{0.1}$Ti$_{0.9}$O$_x$/HZSM-5 with different SiO$_2$/Al$_2$O$_3$ ratios. Reaction conditions: T = 320°C, P = 3.0 MPa, H$_2$/CO$_2$/Ar = 72/24/4 and GHSV = 1500 mL g$_{cat.}$$^{-1}$ h^{-1}.

The influence of reaction conditions for ZnTiOx/HZSM-5-(100): (B) reaction temperature, (C) reaction pressure and (D) GHSV. Reaction conditions: 320°C (except (B)), 3.0 MPa (except (C)), GHSV = 2250 mL g$_{cat.}$$^{-1}$ h^{-1} (except (D)), the H$_2$/CO$_2$/Ar = 72/24/4.

(E)The long-term performance of CO$_2$ hydrogenation to aromatics over Zn$_{0.1}$Ti$_{0.9}$O$_x$/HZSM-5-(100). Reaction conditions: T = 320°C, P = 3.0 MPa, H$_2$/CO$_2$/Ar = 72/24/4 and GHSV = 2250 mL g$_{cat.}$$^{-1}$ h^{-1}.

selected area illustrates the presence of well dispersed Zn element. Also, Zn$_{0.1}$Ti$_{0.9}$O$_x$ is distributed uniform on the zeolite (Figure 2C). Combined with the EDS result, the small particle can be assigned to Zn$_{0.1}$Ti$_{0.9}$O$_x$, and the hexagonal prism is HZSM-5.

The density and strength of the acid sites in HZSM-5 are considered the major factors that affect the distribution of the product in the CTA process. To investigate the acid properties of HZSM5-(x), magic-angle spinning nuclear magnetic resonance (MAS NMR) and NH$_3$-TPD were utilized. In the ^{27}Al MAS NMR spectra of HZSM-5-(x) (Figure 2D), the peak appeared at a chemical shift of 54 ppm is attributed to the four-coordinated aluminum in the framework, which is the primary source of Brønsted acid. The peak intensity of four-coordinated aluminum constantly decreased with the increase of the SiO$_2$/Al$_2$O$_3$ ratio, suggesting the decline of Brønsted acid sites. In HZSM5-(25), there is an obvious small peak at 0 ppm, which is attributed to a trace amount of extra-framework six-coordinated Al.[12,24,25] The ^{29}Si MAS NMR spectra of HZSM-5-(x) were also analyzed (supplemental information, Figure S8). All samples have a peak at −112 ppm attributed to Si in the framework coordinated with four -OSi (denoted as Si (0Al)). The shoulder at the chemical shift of −116 ppm belonged to the crystallographic non-equivalent positions of Si (0Al). The weak peak at −107 ppm is attributed to Si coordinated with an -OAl in the framework (Si(1Al)), representing the aluminum content in the zeolite. In addition, the samples with SiO$_2$/Al$_2$O$_3$ ratios of 100, 130, and 300 also show a weaker peak at −103 ppm, which may partially contribute to the silanol group.[26,27] The results of ^{29}Si MAS NMR spectra are consistent with XRF characterization. The acid properties of HZSM-5-(x) were further measured by NH$_3$-TPD. A set of combined desorption peaks in the relatively low desorption temperature (50–250°C) and two groups of desorption peaks in the relatively high desorption temperature (250–550°C, >550°C)
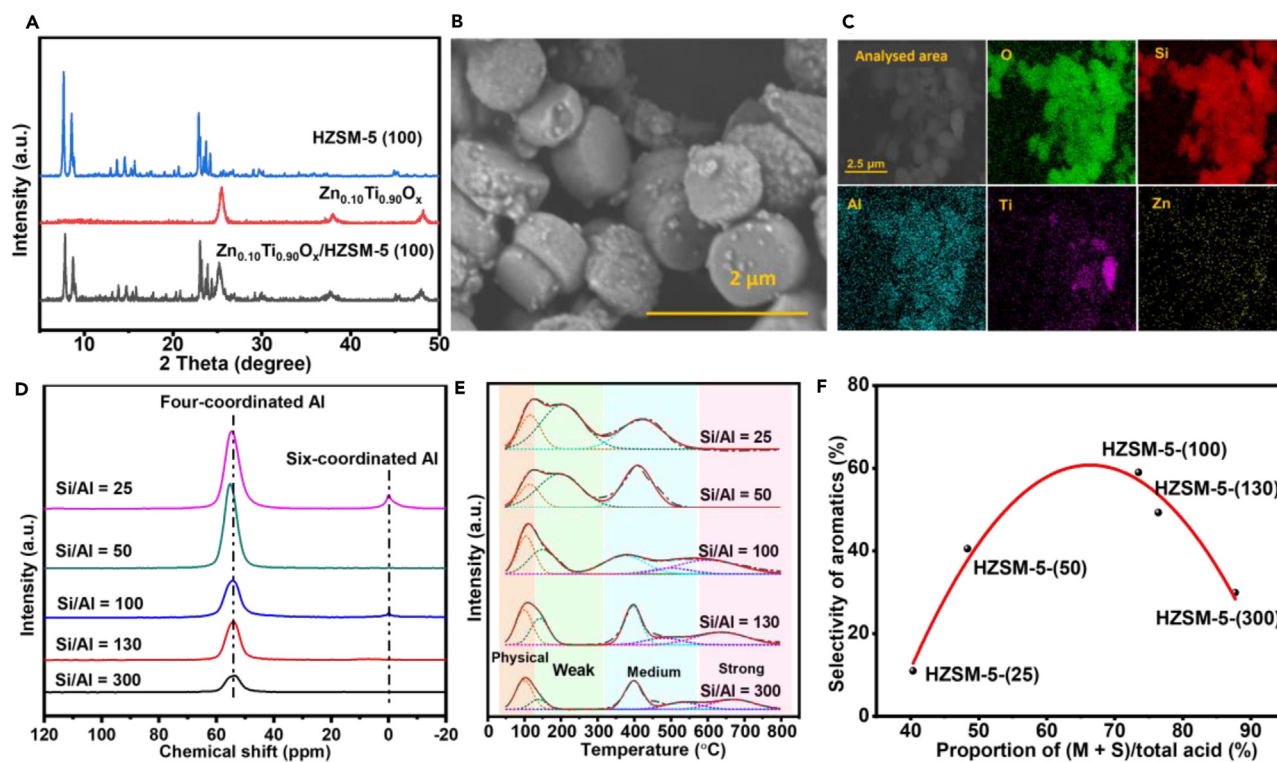
Figure 2. The structure and acid properties of $Zn_{0.1}Ti_{0.9}O_x$/HZSM-5-(x) catalyst

(A) The XRD patterns of $Zn_{0.1}Ti_{0.9}O_x$/HZSM-5-(100) and standard $Zn_{0.1}Ti_{0.9}O_x$ and HZSM-5-(100).

(B) The FE-SEM image of $Zn_{0.1}Ti_{0.9}O_x$/HZSM-5-(100).

(C) The EDS mapping for elements analysis of $Zn_{0.1}Ti_{0.9}O_x$/HZSM-5-(100).

(D) ^{27}Al MAS NMR spectra of HZSM-5-(x).

(E) The deconvoluted NH_3-TPD curves of HZSM-5-(x).

(F) The aromatic selectivity function to the proportion of medium and strong acid in all acid sites. The M + S is short for the medium and strong acid in the picture.

may be observed in the NH_3-TPD curves over all samples (supplemental information, Figure S9). As the increase of SiO_2/Al_2O_3 ratio, the intensity of the desorption peaks at 50–550°C gradually decreases. The deconvoluted NH_3-TPD curves (Figure 2E) show that the peak below 100°C is classified as the physically adsorbed NH_3, and the peak centers at 140–200°C, 400–550°C and 600°C are classified as the weak, medium-strong and strong acid sites on the HZSM-5, respectively. The chemical adsorbed peaks were also quantified (supplemental information, Table S3). With the increase of the SiO_2/Al_2O_3 ratio, the amount of total acid and the weak and strong acids gradually decrease, and the desorption temperature of NH_3 over the strong acid gradually moves to a higher temperature. However, the proportion of medium-strong acids and strong acids to the total amount of acids increases. Combined with the reaction result, the selectivity of aromatics functioned to medium and strong acid proportions conformed to the "volcanic curve" (Figure 2F). Generally, it is thought that the proper ratio of medium and strong acids facilitates the formation of the aromatic. Too many medium and strong acids result in hydrogenolysis to light olefins.[8]

Aromatics are a large family with various homologues, isomers, and substituent groups.[28] BTX are the most valuable aromatic compounds and vital building blocks in the industry.[4–6,11,29] Therefore, improving the proportion of BTX in formed aromatics is essential for the CTA reaction. The product distribution of aromatics over $Zn_{0.1}Ti_{0.9}O_x$/HZSM-5-(100) is listed in supplemental information, Table S4.

The results show that the aromatics formed are mainly heavy ones: the proportions of A_9 and A_{10+} (aromatics contain 9 and at least 10 carbon atoms) are 23.4% and 68.6%, respectively. The selectivity of BTX is only 8.0%. The molecular diameter of A_9 is around 6.5 Å, which is larger than the pore size of HZSM-5, 5.5 Å. Thus, the formation of A_9 or A_{10+} is thought to be on the external surface of HZSM-5. Also, a report demonstrated that heavy aromatics are generated by the further alkylation of light aromatic catalyzed over the acid sites on the pore mouth and the external surface of zeolite.[4] To prevent further alkylation and increase the amount of BTX, TEOS was employed to block the acid sites on the pore mouth and the external surface of HZSM-5. Since the dynamic diameter of TEOS is 10.3 Å, it is impossible to interact with the inner surface of HZSM-5.[22] The TEOS-modified HZSM-5-(100) was characterized by FT-IR (Figure 3A). With silylation, a clear band at $3660 \, cm^{-1}$ appears, which correlates to the hydroxyl vibration of Si-OH. The appearance of the vibration at $3660 \, cm^{-1}$ demonstrates that the SiO_2 was successfully deposited on the external surface of HZSM-5-(100) and formed Si-OH.[30] The characterizations of TEOS-treated HZSM-5 were also conducted (supplemental information, Figures S10–S15, Table S5). XRD results suggest that the structure of HZSM-5 remain intact after TEOS treatment. Al 2p XPS spectra of the HZSM-5-(100) before and after TEOS treatment indicate the surface Al site is gradually covered
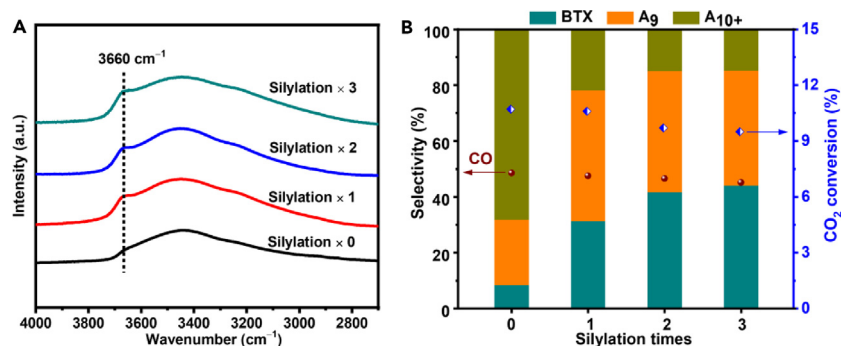
Figure 3. Silylation treated $Zn_{0.1}Ti_{0.9}O_x$/HZSM-5-(100) catalyst
(A) FT-IR spectra of HZSM-5-(100) zeolite modified by TEOS.
(B) After different silylation treatment times, the aromatics distribution over $Zn_{0.1}Ti_{0.9}O_x$/HZSM-5-(100) catalyst. Reaction conditions: T = 320°C, P = 3.0 MPa, $H_2/CO_2/Ar$ = 72/24/4 and GHSV = 2250 mL $g_{cat.}^{-1}$ h^{-1}.

by the TEOS. The SEM, HRTEM and EDS-Mapping results show that the surface of the HZSM-5-(100) becomes slightly rough after TEOS treatments, which may be caused by the amorphous SiO_2 on the external surface. The N_2 absorption-desorption isotherms show that the porous HZSM-5 remained after TEOS treatment. The surface area did not change significantly. These results indicated that the SiO_2 is deposited on the external surface of HZSM-5-(100). Then, the catalytic performances of $Zn_{0.1}Ti_{0.9}O_x$/HZSM-5-(100) after different times of TEOS modification were elucidated (Figure 3B and supplemental information, Table S4). After the first TEOS modification, the proportion of BTX significantly increases to 31.3% and further improves to 41.7% after the second time. After the third time modification, the proportion of BTX reaches 44.1%, and CO_2 conversion slightly decreases to 9.5%. The corresponding BTX selectivity in the overall CTA reaction is ca. 24.1%, showing a comparable BTX selectivity.

Investigation of surface species and reaction mechanism

The reverse water gas shift reaction (RWGS) is the primary side reaction during CO_2 hydrogenation. The selectivity of CO can even reach 40–60% in the CTA process. However, the CO can also be converted to CO_2 through the water gas shift reaction (WGS) at certain reaction conditions, as in the CO hydrogenation reaction. Therefore, revealing the conversion route of CO_2 and CO hydrogenation is crucial for understanding and improving the selectivity of the target product. Then, the catalytic performances of CO_2 and CO hydrogenation over the $Zn_{0.1}Ti_{0.9}O_x$ and the $Zn_{0.1}Ti_{0.9}O_x$/HZSM-5-(100) catalyst under the same reaction conditions have been studied. *In-situ* DRIFTS was applied to monitor the generated species during the reactions (Figure 4, supplemental information, Figures S3 and S16–S18). The result shows that the main product of CO_2 hydrogenation is aromatics at relatively low temperatures (Figure 4A). However, for CO hydrogenation, the selectivity of aromatics is less than 10%, and the main products are light alkanes and light olefins (Figure 4B). Thus, CO_2 forms aromatics directly rather than converts to CO and then transforms to aromatics indirectly.

In-situ DRIFTS was employed to study the evolution of the surface species during the reaction with time variation. The H_2/CO_2 mixture is introduced into the *in-situ* cell with $Zn_{0.1}Ti_{0.9}O_x$/HZSM-5-(100) as a catalyst. The spectra were constantly collected until the reaction reached equilibrium after 30 min. When the H_2/CO_2 mixture is used as the reactant (Figure 4C, supplemental information, Figure S18), two vibrations first appear at 1518 and 1381 cm^{-1}, which correlate to the vibration of carbonate (CO_3^*) and the bending (δ (CH)) of the C–H bond of HCOO*, respectively. With the reaction processing, the vibration peaks appear at 1573 and 1367 cm^{-1} due to the asymmetry and symmetry vibration of the O=C-O group from bidentate formate (b-HCOO*). The peak at 2978 cm^{-1} is attributed to the vibration of methoxy (CH_3O^*). The peak at 2882 cm^{-1} belongs to the stretching vibration (ν(CH)) of the C-H bond of HCOO*.[31–34] According to the intensity change of each peak with the reaction time, the reaction pathway can be predicted as CO_2 firstly adsorbs on the catalyst surface and forms carbonate. Carbonate is then reduced to formate and further hydrogenated to methoxy (supplemental information, Figure S18A). Among the formed species, the amount of the formate is the highest when the reaction reaches equilibrium. Therefore, CO_2 hydrogenation favors the formate route, which can be deduced in our studied reaction condition. When inleting the H_2/CO reactants, the change of DRIFTS with the reaction time differs from those for the H_2/CO_2 reactants (supplemental information, Figure S18B). The intensity of each peak reaches equilibrium after 5 min, and the carbonate species dominate on the surface without significant methoxyl species formation as time goes on. Thus, *in-situ* DRIFTS results further demonstrate that CO_2 forms aromatics directly rather than converting to CO and subsequently forming aromatics indirectly.

However, the direct formation of aromatics from CO_2 hydrogenation is thermodynamically unfavorable (supplemental information, Figure S19). In this work, methanol or light olefins are thermodynamically favorable to form aromatics under reaction conditions. Therefore, methanol or light olefins can be an intermediate to drive CO_2 hydrogenation to aromatics. Combining the acid properties and catalytic performance of $Zn_{0.1}Ti_{0.9}O_x$/HZSM-5 and HZSM-5 (Figure 4D), it may be predicted that methanol is generated over $Zn_{0.1}Ti_{0.9}O_x$ and further converted to light aromatics on the medium and strong acid sites in the channel of HZSM-5. With the acid sites on the external surface blocked by TEOS, the light aromatics may not be further alkylated to heavy aromatics. Then, the direct hydrogenation of CO_2 to aromatics with high aromatics (BTX) selectivity and excellent stability is achieved over a tandem catalyst $Zn_{0.1}Ti_{0.9}O_x$/HZSM-5-(100).
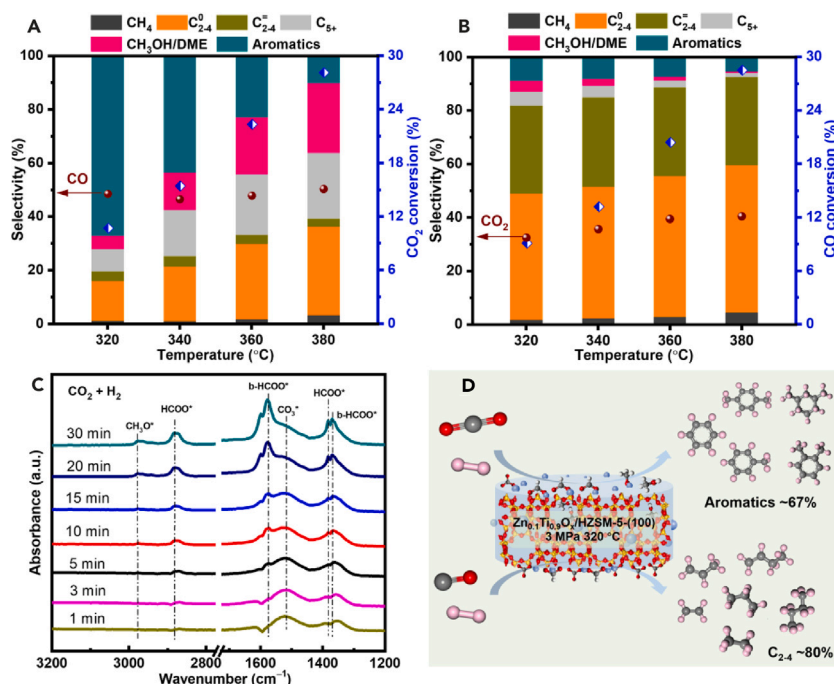
Figure 4. Mechanism study of CO_2 and CO hydrogenation on $Zn_{0.1}Ti_{0.9}O_x$/HZSM-5-(100) catalyst

(A) CO_2 hydrogenation. Reaction conditions: P = 3.0 MPa, H_2/CO_2/Ar = 72/24/4 and GHSV = 1500 mL $g_{cat.}^{-1}$ h^{-1}.

(B) CO hydrogenation. Reaction conditions: P = 3.0 MPa, H_2/CO/Ar = 76/19/5 and GHSV = 1500 mL $g_{cat.}^{-1}$ h^{-1}.

(C) *In-situ* DRIFTS spectra of $Zn_{0.1}Ti_{0.9}O_x$/HZSM-5-(100) catalyst exposed in H_2/CO_2 mixture.

(D) The diagram of the predicted reaction route for CO_2 and CO hydrogenation over $Zn_{0.1}Ti_{0.9}O_x$/HZSM-5-(100).

DISCUSSION

In conclusion, on the tandem $Zn_{0.1}Ti_{0.9}O_x$/HZSM-5-(100) catalyst with the proper amount and ratio of medium and strong acids, the highest aromatics selectivity of 67.2% and CO_2 conversion of 10.7% in the direct CTA reaction are achieved. The catalyst also shows robust stability without deactivation during the 100-h reaction. Blocking the external acid sites of HZSM-5-(100) by TEOS has significantly improved the BTX selectivity. The highest selectivity of BTX, up to 24.1%, may be achieved after three times of TEOS-modification. The primary mechanism study demonstrates that CO_2 hydrogenation is under the formate route. The major surface species is formate, which differs from the carbonate in CO hydrogenation. This study may provide an efficient catalyst design route for CO_2 hydrogenation to value-added products.

Limitations of the study

In this work, a tandem catalyst $Zn_{0.1}Ti_{0.9}O_x$/HZSM-5-(100) catalysts with appropriate density and strength of acid sites exhibit a high aromatics selectivity and long-term stability. The detailed reaction route over metal oxide was investigated, but the carbon-carbon coupling mechanism over acid sites was not deeply studied in this work. The theoretical calculation is also required to elucidate the mechanistic pathways over tandem catalysts in the future.

STAR★METHODS

Detailed methods are provided in the online version of this paper and include the following:

- KEY RESOURCES TABLE
- RESOURCE AVAILABILITY
  - Lead contact
  - Materials availability
  - Data and code availability
- EXPERIMENTAL MODEL AND STUDY PARTICIPANT DETAILS
- METHOD DETAILS
  - Materials
  - Catalyst preparation

- ○ Catalyst characterisations
- ○ Catalytic testing
- ○ The Weisz-Prater criterion (θ_G) calculating

AUTHOR CONTRIBUTIONS

L.Y., B.Y., and H.H. supervised the project and designed the research. J.Z. and Y.M. performed the synthesis, characterizations and catalytic test. H.D. performed NMR measurements and analysis. Y.R. assisted with material characterizations. All authors discussed the results and commented on the manuscript.

DECLARATION OF INTERESTS

The authors declare no competing interests.

REFERENCES

1. Álvarez, A., Bansode, A., Urakawa, A., Bavykina, A.V., Wezendonk, T.A., Makkee, M., Gascon, J., and Kapteijn, F. (2017). Challenges in the greener production of formates/formic acid, methanol, and DME by heterogeneously catalyzed CO_2 hydrogenation processes. Chem. Rev. 117, 9804–9838. https://doi.org/10.1021/acs.chemrev.6b00816.

2. Kar, S., Sen, R., Goeppert, A., and Prakash, G.K.S. (2018). Integrative CO_2 capture and hydrogenation to methanol with reusable catalyst and amine: Toward a carbon neutral methanol economy. J. Am. Chem. Soc. 140, 1580–1583. https://doi.org/10.1021/jacs.7b12183.

3. Li, M.M.-J., and Tsang, S.C.E. (2018). Bimetallic catalysts for green methanol production via CO_2 and renewable hydrogen: a mini-review and prospects. Catal. Sci. Technol. 8, 3450–3464. https://doi.org/10.1039/C8CY00304A.

4. Cheng, K., Zhou, W., Kang, J., He, S., Shi, S., Zhang, Q., Pan, Y., Wen, W., and Wang, Y. (2017). Bifunctional catalysts for one-step conversion of syngas into aromatics with excellent selectivity and stability. Chem 3, 334–347. https://doi.org/10.1016/j.chempr.2017.05.007.

5. Huang, Z., Wang, S., Qin, F., Huang, L., Yue, Y., Hua, W., Qiao, M., He, H., Shen, W., and Xu, H. (2018). Ceria-zirconia/zeolite bifunctional catalyst for highly selective conversion of syngas into aromatics. ChemCatChem 10, 4519–4524. https://doi.org/10.1002/cctc.201800911.

6. Zhao, B., Zhai, P., Wang, P., Li, J., Li, T., Peng, M., Zhao, M., Hu, G., Yang, Y., Li, Y.-W., et al. (2017). Direct transformation of syngas to aromatics over Na-Zn-Fe₅C₂ and hierarchical HZSM-5 tandem catalysts. Chem 3, 323–333.

7. Shen, K., Qian, W., Wang, N., Su, C., and Wei, F. (2014). Centrifugation-free and high yield synthesis of nanosized H-ZSM-5 and its structure-guided aromatization of methanol to 1,2,4-trimethylbenzene. J. Mater. Chem. A 2, 19797–19808. https://doi.org/10.1039/C4TA04444D.

8. Wang, Y., Gao, W., Kazumi, S., Li, H., Yang, G., and Tsubaki, N. (2019). Direct and oriented conversion of CO_2 into value-added aromatics. Chem. Eur J 25, 5149–5153. https://doi.org/10.1002/chem.201806165.

9. Li, Z., Qu, Y., Wang, J., Liu, H., Li, M., Miao, S., and Li, C. (2019). Highly Selective Conversion of Carbon Dioxide to Aromatics over Tandem Catalysts. Joule 3, 570–583. https://doi.org/10.1016/j.joule.2018.10.027.

10. Chang, C., Lang, W.H., and Silvestri, A.J. (1979). Synthesis gas conversion to aromatic hydrocarbons. J. Catal. 56, 268–273. https://doi.org/10.1016/0021-9517(79)90113-1.

11. Lyons, T.W., Guironnet, D., Findlater, M., and Brookhart, M. (2012). Synthesis of p-xylene from ethylene. J. Am. Chem. Soc. 134, 15708–15711. https://doi.org/10.1021/ja307612b.

12. Yang, J., Pan, X., Jiao, F., Li, J., and Bao, X. (2017). Direct conversion of syngas to aromatics. Chem. Commun. 53, 11146–11149. https://doi.org/10.1039/C7CC04768A.

13. Kuei, C.-K., and Lee, M.-D. (1991). Hydrogenation of carbon dioxide by hybrid catalysts, direct synthesis of aromatics from carbon dioxide and hydrogen. Can. J. Chem. Eng. 69, 347–354. https://doi.org/10.1002/cjce.5450690142.

14. Ni, Y., Chen, Z., Fu, Y., Liu, Y., Zhu, W., and Liu, Z. (2018). Selective conversion of CO_2 and H_2 into aromatics. Nat. Commun. 9, 3457. https://doi.org/10.1038/s41467-018-05880-4.

15. Wang, Y., Kazumi, S., Gao, W., Gao, X., Li, H., Guo, X., Yoneyama, Y., Yang, G., and Tsubaki, N. (2020). Direct conversion of CO_2 to aromatics with high yield via a modified Fischer-Tropsch synthesis pathway. Appl. Catal. B Environ. 269, 118792. https://doi.org/10.1016/j.apcatb.2020.118792.

16. Wang, Y., Tan, L., Tan, M., Zhang, P., Fang, Y., Yoneyama, Y., Yang, G., and Tsubaki, N. (2019). Rationally designing bifunctional catalysts as an efficient strategy to boost CO_2 hydrogenation producing value-added aromatics. ACS Catal. 9, 895–901. https://doi.org/10.1021/acscatal.8b01344.

17. Zhou, J., Ye, L., Huang, D., Wang, M., Ren, Y., Yue, B., and He, H. (2021). The synergy of modulated surface polarity and oxygen vacancy for CO_2 to methanol over Zn$^{(δ−)}$-Ti$^{(δ+)}$Ovacancy. J. Energy Chem. 56, 449–454. https://doi.org/10.1016/j.jechem.2020.08.021.

18. Wang, S., Zhang, L., Wang, P., Jiao, W., Qin, Z., Dong, M., Wang, J., Olsbye, U., and Fan, W. (2022). Highly selective hydrogenation of CO_2 to propane over GaZrO$_x$/H-SSZ-13 composite. Nat. Catal. 5, 1038–1050. https://doi.org/10.1038/s41929-022-00871-7.

19. Zhang, L., Fu, T., Ren, K., Han, Y., Wang, R., Zhan, G., and Li, Z. (2023). Finely regulating methanol concentration to control the alkylation depth in methanol aromatization for optimizing product distribution. Appl. Catal. B Environ. 321, 122047. https://doi.org/10.1016/j.apcatb.2022.122047.

20. Schmidt, J.E., Poplawsky, J.D., Mazumder, B., Attila, Ö., Fu, D., de Winter, D.A.M., Meirer, F., Bare, S.R., and Weckhuysen, B.M. (2016). Coke formation in a zeolite crystal during the methanol-to-hydrocarbons reaction as

studied with atom probe tomography. Angew. Chem. Int. Ed. *55*, 11173–11177. https://doi.org/10.1002/anie.201606099.

21. Qi, L., Li, J., Wang, L., Wang, C., Xu, L., and Liu, Z. (2017). Comparative investigation of the deactivation behaviors over HZSM-5 and HSAPO-34 catalysts during low-temperature methanol conversion. Catal. Sci. Technol. *7*, 2022–2031. https://doi.org/10.1039/C7CY00024C.

22. Qi, L., Li, J., Wang, L., Xu, L., and Liu, Z. (2017). Unusual deactivation of HZSM-5 zeolite in the methanol to hydrocarbon reaction. Catal. Sci. Technol. *7*, 894–901. https://doi.org/10.1039/C6CY02459A.

23. Zheng, S., Heydenrych, H.R., Jentys, A., and Lercher, J.A. (2002). Influence of surface modification on the acid site distribution of HZSM-5. J. Phys. Chem. B *106*, 9552–9558. https://doi.org/10.1021/jp014091d.

24. Shaikh, R.A., Hegde, S.G., Behlekar, A.A., and Rao, B.S. (1999). Enhancement of acidity and paraselectivity by the silynation in pentasil zeolites. Catal. Today *49*, 201–209. https://doi.org/10.1016/S0920-5861(98)00425-8.

25. van Bokhoven, J.A., Koningsberger, D.C., Kunkeler, P., van Bekkum, H., and Kentgens, A.P.M. (2000). Stepwise dealumination of zeolite beta at specific T-sites observed with ^{27}Al MAS and ^{27}Al MQ MAS NMR. J. Am. Chem. Soc. *122*, 12842–12847. https://doi.org/10.1021/ja002689d.

26. Ma, D., Shu, Y., Han, X., Liu, X., Xu, Y., and Bao, X. (2001). Mo/HMCM-22 catalysts for methane dehydroaromatization: A multinuclear MAS NMR study. J. Phys. Chem. B *105*, 1786–1793. https://doi.org/10.1021/jp002011k.

27. Batamack, P., Doremieux-Morin, C., Fraissard, J., and Freude, D. (1991). Broad-line and high-resolution NMR studies concerning the hydroxonium ion in HZSM-5 zeolites. J. Phys. Chem. *95*, 3790–3796. https://doi.org/10.1021/j100162a064.

28. Niziolek, A.M., Onel, O., and Floudas, C.A. (2016). Production of benzene, toluene, and xylenes from natural gas via methanol: Process synthesis and global optimization. AIChE J. *62*, 1531–1556. https://doi.org/10.1002/aic.15144.

29. Zhang, P., Tan, L., Yang, G., and Tsubaki, N. (2017). One-pass selective conversion of syngas to para-xylene. Chem. Sci. *8*, 7941–7946. https://doi.org/10.1039/C7SC03427J.

30. Ding, H., Ding, J., Liu, W., Zhao, X., Chi, Q., Zhu, K., Zhou, X., and Yang, W. (2019). A phase-transfer crystallization pathway to synthesize ultrasmall silicoaluminophosphate for enhanced catalytic conversion of dimethylether-to-olefin. CrystEngComm *21*, 577–582. https://doi.org/10.1039/C8CE01752B.

31. Chen, K., Fang, H., Wu, S., Liu, X., Zheng, J., Zhou, S., Duan, X., Zhuang, Y., Chi Edman Tsang, S., and Yuan, Y. (2019). CO2 hydrogenation to methanol over Cu catalysts supported on La-modified SBA-15: The crucial role of Cu–LaOx interfaces. Appl. Catal. B Environ. *251*, 119–129. https://doi.org/10.1016/j.apcatb.2019.03.059.

32. Duyar, M.S., Tsai, C., Snider, J.L., Singh, J.A., Gallo, A., Yoo, J.S., Medford, A.J., Abild-Pedersen, F., Studt, F., Kibsgaard, J., et al. (2018). A highly active molybdenum phosphide catalyst for methanol synthesis from CO and CO$_2$. Angew. Chem. Int. Ed. *57*, 15045–15050. https://doi.org/10.1002/anie.201806583.

33. Wang, J., Li, G., Li, Z., Tang, C., Feng, Z., An, H., Liu, H., Liu, T., and Li, C. (2017). A highly selective and stable ZnO-ZrO$_2$ solid solution catalyst for CO$_2$ hydrogenation to methanol. Sci. Adv. *3*, e1701290. https://doi.org/10.1126/sciadv.1701290.

34. Kattel, S., Yan, B., Yang, Y., Chen, J.G., and Liu, P. (2016). Optimizing binding energies of key intermediates for CO$_2$ hydrogenation to methanol over oxide-supported copper. J. Am. Chem. Soc. *138*, 12440–12450. https://doi.org/10.1021/jacs.6b05791.

35. García, J.R., Bidabehere, C.M., and Sedran, U. (2017). Diffusion controlled LHHW kinetics. Simultaneous determination of chemical kinetic and equilibrium adsorption constants by using the Weisz-Prater approach. Chem. Eng. Sci. *172*, 444–452. https://doi.org/10.1016/j.ces.2017.06.048.

36. Golchoobi, A., and Pahlavanzadeh, H. (2016). Molecular simulation, experiments and modelling of single adsorption capacity of 4A molecular sieve for CO$_2$–CH$_4$ separation. Sep. Sci. Technol. *51*, 2318–2325. https://doi.org/10.1080/01496395.2016.1206571.

37. Zhang, M., Qian, W., Ma, H., Ying, W., Zhang, H., and Yuan, P. (2023). A theoretical study on the separation of CO$_2$/CH$_4$ through MFI zeolite. Comput. Theor. Chem. *1228*, 114272. https://doi.org/10.1016/j.comptc.2023.114272.

38. Jobic, H., and Theodorou, D.N. (2007). Quasi-elastic neutron scattering and molecular dynamics simulation as complementary techniques for studying diffusion in zeolites. Microporous Mesoporous Mater. *102*, 21–50. https://doi.org/10.1016/j.micromeso.2006.12.034.

39. García-Sánchez, J.T., Valderrama-Zapata, R., Acevedo-Córdoba, L.F., Pérez-Martínez, D., Rincón-Ortiz, S., and Baldovino-Medrano, V.G. (2023). Calculation of Mass Transfer Limitations for a Gas-Phase Reaction in an Isothermal Fixed Bed Reactor: Tutorial and Sensitivity Analysis. ACS Catal. *13*, 6905–6918. https://doi.org/10.1021/acscatal.3c01282.

STAR★METHODS

KEY RESOURCES TABLE

REAGENT or RESOURCE	SOURCE	IDENTIFIER
Chemicals, peptides, and recombinant proteins		
$Zn(NO_3)_2 \cdot 6H_2O$	Sinopgarm Chemical Regent Co., Ltd	Cat#80141318; CAS: 10196-18-6
$Ti(SO_4)_2$	Sinopgarm Chemical Regent Co., Ltd	Cat#20044418; CAS: 13693-11-3
$(NH_4)_2CO_3$	Sinopgarm Chemical Regent Co., Ltd	Cat#100001418; CAS: 10361-29-2
HZSM-5	Nankai University Catalyst CO., Ltd.	N/A
TPAOH	Aladdin Industrial CO., Ltd.	Cat#T501277; CAS: 4499-86-9
$NaAlO_2$	Sinopgarm Chemical Regent Co., Ltd	Cat#XW1113849102; CAS: 11138-49-1
$CO_2/H_2/Ar$	Air liquide	N/A
$CO/H_2/Ar$	Air liquide	N/A
D_2	Newrad Specialty Gases Co., Ltd	N/A
Other		
Stainless steel fixed-bed in continuous flow	Tianjin Golden Eagle Technology Co.,Ltd	N/A
GC	HUAAI CHROMATOGRAPHY	N/A

RESOURCE AVAILABILITY

Lead contact

Further information and requests for resources should be directed to and will be fulfilled by the lead contact, Lin Ye (yelin@fudan.edu.cn).

Materials availability

The study did not generate new unique materials. The readers can buy the chemicals to remake the materials as mentioned in the text.

Data and code availability

Date: The datasets generated during this study are available from the lead contact upon request.

Code: This paper does not report the original code.

Any additional information required to reanalyse the data reported in this paper is available from the lead contact upon request.

EXPERIMENTAL MODEL AND STUDY PARTICIPANT DETAILS

This study does not use experimental models.

METHOD DETAILS

Materials

Commercial HZM-5 with SiO_2/Al_2O_3 ratio of 25, 130, and 300 were purchased from Nankai University Catalyst CO., Ltd and denoted as HZSM-5-(x), where x represents the SiO_2/Al_2O_3 ratio. $Zn(NO_3)_2 \cdot 6H_2O$ (AR), $Ti(SO_4)_2$ (AR), $(NH_4)_2CO_3$ (AR), and $NaAlO_2$ (AR) were purchased from Sinopgarm Chemical Regent Co., Ltd. And the TPAOH was purchased from Aladdin Industrial Co., Ltd without further purification. The gas mixture $CO_2/H_2/Ar$ and $CO/H_2/Ar$ were purchased from Air Liquide. D_2 was purchased from Newrad Specialty Gases Co., Ltd. All chemicals were used without further purification.

Catalyst preparation

The bimetallic oxides of $Zn_{0.1}Ti_{0.9}O_x$ were prepared *via* the co-precipitation method. In a typical synthesis procedure, 0.594 g of $Zn(NO_3)_2 \cdot 6H_2O$ and 4.32 g of $Ti(SO_4)_2$ were dissolved in 100 mL of distilled water to obtain a transparent solution, and the total concentration of metal ions was 0.2 M. The solution was heated to 70°C, and then 1 M $(NH_4)_2CO_3$ aqueous solution was added slowly with vigorous stirring. The resulting white gel was further aged for 3 h at the same temperature. The mixture was further filtrated, washed repeatedly, dried at 100°C overnight and calcined in static air at 500°C for 5 h.

Besides the purchased HZSM-5-25, HZSM-5-130, and HZSM-5-300, two samples of HZSM-5-50 and HZSM-5-100 were hydrothermal synthesised. Typically, the molar composition of the precursor gel was $1.0SiO_2$: xAl_2O_3: $0.4TPAOH$: $55H_2O$ (x = 0.01 or 0.02). Tetraethyl

orthosilicate (TEOS) and NaAlO$_2$ were used as silicon and aluminium source materials, respectively. Tetrapropylammonium hydroxide (TPAOH) was used as the organic structure-directing agent and dissolved in deionised water. Then, the desired amount of NaAlO$_2$ was added to the solution and stirred for 1 h. TEOS was further added dropwise, and the mixture was stirred for 12 h. The resulting gel was transferred into a 200 mL Teflon-lined stainless steel autoclave and crystallised at 180°C for 48 h. After filtration and washing with deionised water, the resulting product was dried at 100°C overnight and calcined at 550°C for 5 h.

The HZSM-5 samples modified by TEOS were denoted as HZSM-5-Si × n, where n represented the treatment cycles. The brief procedure was as follows: 1g of TEOS was dissolved in 5 mL hexane, and 2 g of as-synthesised HZSM-5-(100) was added to the solution. The mixture was further stirred at room temperature for 24 h. After that, the sample was dried at 100°C overnight and calcined at 550°C for 4 h. This TEOS modification procedure was repeated several times.

The tandem catalyst of bimetal oxide Zn$_{0.1}$Ti$_{0.9}$O$_x$ coupled with HZSM-5 was prepared via the physical grinding method. Typically, the powders of obtained Zn$_{0.1}$Ti$_{0.9}$O$_x$ and HZSM-5 were mixed in agate mortar at the mass ratio of 1 : 1 unless otherwise stated. The mixture was further ground for 10 min. The obtained catalyst was pressed into tablets and crushed into particles with 40~60 messes before evaluation.

Catalyst characterisations

X-ray diffraction (XRD) patterns were recorded on a Bruker D8 Advances diffractometer using Cu-Kα radiation (λ = 0.15418 nm) at 40 kV and 40 mA with a scanning angle (2θ) ranging from 5° to 80°. The step size was 0.02° with a counting rate of 0.2 ~ 0.8 s per step. X-ray fluorescence (XRF) spectroscopy was used to analyse the elemental content on a Bruker S4 EXPLORER XRF spectrometer.

The N$_2$ adsorption–desorption isotherms were measured at -196°C using a Micromeritics TriStar II 3020 porosimetry analyser. The samples were degassed at 300°C for 3 h before the measurements to remove physically adsorbed impurities. The specific surface area (S_{BET}) was calculated according to the Brunauer–Emmett–Teller (BET) method, and the total pore volume (V_{pore}) was derived from the adsorbed N$_2$ volume at a relative pressure of approximately 0.99.

The thermogravimetry analysis (TGA) was carried out on a TA SDT Q600 analyser. The sample was tested in air from room temperature to 800°C at a rate of 5°C min^{-1}. After long-term performance evaluation (100 h), the retained species were investigated by the gas chromatography-mass spectrometry (GC-MS) operated on a PE 680-ST8 GC-MS analyser. The used catalyst was immersed in dichloromethane for 2 h and then ultrasonic treated for 30 min, and this operation was repeated twice. The obtained extraction liquid was concentrated by rotary evaporation, denoted as outside. After neutralisation, the remaining catalyst sample was then dissolved by hydrofluoric acid and extracted by dichloromethane. After that, the extraction liquid was also concentrated by rotary evaporation, denoted as the sample inside. Finally, these two concentrated samples were analysed with GC-MS.

The field-emission SEM (FE-SEM) images and EDS elemental analysis were collected on a FEI Nova NanoSem 450 FE-SEM. The tested samples were carefully ground before being transferred to a conducting resin. The statistical mean diameter of the nanoparticles was measured by counting at least 200 particles.

The X-ray Photoelectron Spectroscopy (XPS) was conducted on the AXIS Kratos Supra$^+$. The binding energy (BE) was calibrated by using C 1s line with BE value of 284.8 eV.

The High-Resolution Transmission Electron Microscope (HRTEM) was collected on the HT7700 Exalens, the accelerating voltage was 200 kV.

NH$_3$-TPD was carried out on a Micromeritics Autochem II 2920 chemisorption instrument, and the desorbed NH$_3$ was detected online by a thermal conductivity detector (TCD). Typically, a 150 mg sample was loaded in a U-shaped quartz tube and dried in a He flow (50 mL min^{-1}) at 300°C for 2 h to remove moisture and impurities. After the temperature cooled to 50°C, a mixed gas of 5%NH$_3$-95%Ar (50 mL min^{-1}) was introduced and adsorbed for 1 h, then the gas was switched to He for at least 30 min. Finally, the NH$_3$-TPD curve was recorded from 50°C to 800°C with a rate of 10°C min^{-1} after the baseline stabilised.

Magic angle spinning nuclear magnetic resonance (MAS NMR) characterisation was performed on a Bruker Advance III 400 WB spectrometer. The single-pulse ^{27}Al MAS NMR spectra were recorded at 104.3 MHz with 0.2 µs (10°) of pulse width and 0.3 s of pulse delay using a 4 mm ZrO$_2$ rotor under a spinning rate of 12 kHz. The single-pulse ^{29}Si MAS NMR spectra were collected at 79.6 MHz with 1.6 µs (30°) of pulse width and 15 s of pulse delay using a 7 mm ZrO$_2$ rotor under a spinning rate of 4 kHz. The external standards for the chemical shifts of ^{27}Al and ^{29}Si were AlCl$_3$ (1 M) and tetramethylsilane, respectively.

FT-IR spectroscopy was conducted on a Nicolet iS10 spectrometer at a resolution of 4 cm^{-1} and the scanning ranged from 400 to 4000 cm^{-1}. *In-situ* diffuse reflectance infrared Fourier transform spectroscopy (DRIFS) was performed on a Nicolet 6700 spectrometer. The catalyst sample was *in-situ* pretreated in H$_2$ at 320°C for 2 h before measurement. The Reaction substrate, such as H$_2$-CO$_2$ mixture (H$_2$/CO$_2$ = 3/1, molar ratio), D$_2$ or H$_2$-CO mixture (H$_2$/CO = 3/1, molar ratio), was allowed to pass through the *in-situ* cell with the total flow rate of 20 mL min^{-1}. IR spectra were continuously recorded every 30 s until the intensity of spectra was steady.

Catalytic testing

The catalytic performance was evaluated in continuous flow mode using a stainless steel fixed-bed reactor. The inside diameter of the quartz tube lining in the tubular reactor was 6 mm. Typically, 800 mg of tandem catalyst (40 to 60 meshes) was loaded into the centre of the reactor, with two sides of the catalyst bed packed with quartz powder (20 to 40 meshes). The catalyst was pretreated *in-situ* with H$_2$ for 2 h at 320°C. A premixed gas was used as the feed with the ratio of H$_2$/CO$_2$/Ar = 72/24/4, in which the Ar was adopted as the internal standard for online gas chromatograph (GC) analysis. Data were collected after at least 3 h on stream.

The outlet stream was sampled using a computer-controlled auto-sampling system consisting of a Valco 6-ports valve and two 10-ports valves, then analysed by two GCs. One Huaai GC-9560 gas chromatograph was equipped with a thermal conductivity detector (TCD) and a flame ionisation detector (FID 1). The other GC was Solution GC-9160, which was fitted with a flame ionisation detector (FID 2). Porapak Q packed column (5 m × 2 mm) linked with a 13X molecular sieves packed column (3 m × 2 mm) and connected to TCD, Al_2O_3/S capillary column (50 m × 0.32 mm ×10 μm) was linked to FID 1, while HP-FFAP capillary column (30 m × 0.32 mm × 1.0 μm) was connected to FID 2. CO_2, CO and Ar were detected by TCD, and light hydrocarbons (such as lower olefins and light alkanes) were analysed by FID 1. Aromatics and oxygenated chemicals (such as CH_3OH and dimethyl ether) were analysed by FID 2. Since the TCD and two FIDs could detect CH_4, methane was used as the second internal standard to calibrate three detectors.

A PE680-ST8 GC-MS system with standard samples was used to confirm the products. The organic products (denoted as $C_iH_jO_k$, k = 0 for the chemicals contain no oxygen) included CH_3OH, CH_3OCH_3 (DME), CH_4 and lower olefins ($C_{2-4}^=$), light alkanes (C_{2-4}^0), paraffin contain at least five carbon atoms (C_{5+}) and aromatics. The conversion of CO_2, the selectivity of CO and organic products were calculated by the following equations:

$$Conversion_{CO_2} = \frac{n_{CO_2 - input} - n_{CO_2 - output}}{n_{CO_2 - input}} \times 100\%$$ (Equation 1)

$$Selectivity_{CO} = \frac{n_{CO - output}}{n_{CO_2 - input} - n_{CO_2 - output}} \times 100\%$$ (Equation 2)

$$Selectivity_{C_iH_jO_k} = \frac{i \times n_{C_iH_jO_k}}{\sum i \times n_{C_iH_jO_k}} \times 100\%$$ (Equation 3)

where the subscripts "input" and "output" denote relevant chemicals in the feed and the outlet stream, respectively, all "n" s represent their molar number. "i" represents the number of carbon atoms in the molecule of organic product. The selectivity of CO is calculated based on the total converted carbon and is not included in organic products. The sum of the selectivity of organic products is 100%.

The carbon balance was calculated as the following equation:

$$Carbon\ balence = \frac{n_{CO_2 - output} + n_{CO - output} + \sum i \times n_{C_iH_jO_k}}{n_{CO_2 - input}} \times 100\%$$ (Equation 4)

The carbon balance was higher than 95% in this study.

The Weisz-Prater criterion (θ_G) calculating

The generalised Weisz-Prater criterion reflects the internal transport limitation for internal diffusion. Based on generalised Weisz-Prater criterion, if $\theta_G \ll 1$, the intra-particle diffusion limitations can be neglected.[35] In our work, the reaction conditions are P = 3 MPa, T = 320°C = 593 K, $H_2/CO_2/Ar$ = 72/24/4, GHSV = 2250 mL $g_{cat.}^{-1}$ h^{-1} = 2250 L $kg_{cat.}^{-1}$ h^{-1}, the catalyst particle size is ca. 0.30 mm (40 - 60 mesh, L = 1.5 × 10^{-4} m), the catalyst density (ρ) is ca. 1785 kg m^{-3} [36]; the CO_2 diffusivity (D_{593}) is 8.7 × 10^{-10} m^2 s^{-1} (which was calculated according to the formula $D = \frac{D_{300}}{\left(\frac{300}{T}\right)^2 \left(\frac{P}{101.325}\right)}$ and referred to the literature, the CO_2 self-diffusion coefficiency at 300 K, (D_{300}) is 0.66 × 10^{-8} m^2 s^{-1} [37,38]) and CO_2 conversion is 10%. The Weisz-Prater criterion (θ_G) in our condition is calculated as 0.213,[39] which suggests the internal transport limitation is negligible. The detailed calculation is as follows:

The concentration of CO_2

$$c = \frac{P}{RT} = \frac{3 \times 10^6\ Pa \times 0.24}{8.314\ J\ mol^{-1}\ K^{-1} \times 593\ K} = 146\ mol\ m^{-3}$$

The reaction rate

$$R = \frac{dn_{CO_2}}{dt} = \frac{2250\ L\ kg_{cat.}^{-1}\ h^{-1} \times 0.24 \times 0.1 \times 1\ h}{22.4\ L\ mol^{-1} \times 3600\ s} \times 1785\ kg\ m^{-3} = 1.20\ mol\ m^{-3}\ s^{-1}$$

The Weisz-Prater criterion (θ_G)

$$\theta_{G=}\Phi^2\eta = \frac{L^2 R}{D_{593}c} = \frac{(1.5 \times 10^{-4}\ m)^2 \times 1.20\ mol\ m^{-3}\ s^{-1}}{8.7 \times 10^{-10}\ m^2\ s^{-1} \times 146\ mol\ m^{-3}} = 0.213 \ll 1$$